(Received 16 December 2023, Accepted 21 January 2024, Scheduled 13 February 2024)

Research on the Control System of Bearingless Induction Motor Based on Improved Active Disturbance Rejection Control

Xiang Wang[1], Zebin Yang[1,*], Xiaodong Sun[2], and Shihan Zhan[1]

[1] School of Electrical Information Engineering, Jiangsu University, Zhenjiang 212013, China
[2] Research Institute of Automotive Engineering, Jiangsu University, Zhenjiang 212013, China

ABSTRACT: To enhance the reaction speed, suspension performance, and anti-interference ability of a Bearingless Induction Motor (BIM) operation control system, an improved Active Disturbance Rejection Control (ADRC) technique is proposed. Firstly, the ADRC in the suspension system and the ADRC in the torque system are designed, respectively, using the BIM's mathematical model as the basis. Furthermore, the error integral signal is incorporated into the nonlinear state error feedback control law of the standard ADRC controller. Subsequently, a novel optimal control function is formulated using the fitting method, which is based on the original *fal* function. This approach effectively mitigates the impact of output signal fluctuations at the inflection point of the *fal* function. Simultaneously, the RBF neural network technique is employed to autonomously adjust the control parameters of the extended state observer, therefore enhancing the system's observation capability. Ultimately, the classic ADRC control strategy and the IADRC strategy are compared through simulation and experimentation. Simulations and experimental findings demonstrate that the suggested control method enhances the BIM control system's response time and resilience to external disturbance. Additionally, it enhances the levitation performance of the BIM system.

1. INTRODUCTION

Magnetic bearing technology is incorporated with an induction motor in a bearingless induction motor (BIM). A set of levitation windings is embedded in the stator slot of the induction motor so that the motor produces a nonuniform air gap magnetic field. The rotation and suspension of the rotor can be realized by controlling the current of the suspension force winding and the torque winding [1–3]. The BIM exhibits attributes such as the absence of mechanical friction, negligible maintenance requirements, extended lifespan, and the absence of pollutants. Consequently, it holds significant potential for applications in aircraft, semiconductors, biochemistry, life science, and other domains [4–6]. To ensure the operation performance of the BIM in a complex application environment, the corresponding stable operation control algorithm is a research hotspot with important engineering significance.

BIM exhibits the attributes of nonlinearity, multivariable nature, and robust coupling. To gain the best static as well as dynamic performance from a BIM, sophisticated control algorithms need to be researched [7, 8]. When there are interference factors in the system or when the degree of nonlinearity grows, the proportion integration differentiation (PID) controller is unable to adapt itself appropriately, leading to a diminished ability to effectively suppress disturbances [9–12]. Hence, the PID controller has challenges in achieving high-performance control when there are variations in parameters and unexpected torque disturbances during motor operation. Consequently, modern control theories have been implemented in the BIM to enhance both dynamic and static performances, as well as improve resistance to disturbances such as sliding mode control [13], model predictive control [14], and internal model control [15]. Nevertheless, the use of the aforementioned approaches to provide stability control of BIM is limited due to the complex and nonlinear nature of the BIM control model [16–18]. Sliding mode control can result in rotor buffeting. Model predictive control significantly increases the computing burden of the controller, and internal model control is applicable only to control objects with modeling errors within a specific range. Therefore, when the above algorithms are used for BIM control, the application effect and control performance will be greatly affected.

Active Disturbance Rejection Control (ADRC) controller exhibits an elevated level of robustness and adaptability because it combines the benefits of PID with modern control theory state observer to efficiently detect and counteract internal as well as external disturbances in a system [19]. Ref. [20] utilized the ADRC method to suppress the vibration of a motor during driving and deceleration and verified the superior control performance of the ADRC method. Existing studies have shown that it is feasible to use the ADRC method to control a BIM and has potential practical application value [21–23]. The control effect can be significantly impacted by the fixed structural features and incorrect parameter configuration of the conventional ADRC controller. Recently, several academics have started enhancing the control structure of the conventional ADRC controller. As an illustration, a study in [24] introduced

* Corresponding author: Zebin Yang (zbyang@ujs.edu.cn).

an improved nonlinear ADRC that incorporates a linear Extended State Observer (ESO) to first gauge the overall perturbation. Convergence and stability of the ADRC are enhanced at the same time when the estimated value is incorporated into the nonlinear ESO through the use of the defined weight regular function. Ref. [25] suggests using a nonlinear phase-locked loop observer as a replacement for the extended state observer in ADRC. The enhanced ADRC is employed in bearingless permanent magnet slice motor systems to provide excellent dynamic, static, and anti-interference capabilities. However, the ADRC controller includes a lot of parameters that are difficult to configure. The control system's effectiveness is greatly impacted by the settings selected. Numerous academics have conducted thorough investigations on parameter tuning, and artificial intelligence algorithms offer a promising approach to address parameter optimization challenges in intricate nonlinear systems [26–29]. Ref. [30] improves the traditional particle swarm optimization technique by utilizing the principles of genetic algorithm theory. With this update, the algorithm's optimization scope and rates of convergence are increased, and the ADRC parameters can be changed online. In comparison to the standard ADRC, it exhibits superior position-tracking capabilities and reduced correction time. Nevertheless, employing a swarm intelligence algorithm to enhance the global parameters of ADRC has challenges in ensuring control effectiveness due to its extensive computational requirements and susceptibility to local convergence. Without depending on the information about the mathematical model of the plant, the radial basis function neural network (RBFNN) approach may be able to determine the underlying nonlinear relationship through training. It only needs a small amount of training data [31–33]. The RBFNN can obtain the adjustment information of controller parameters online and execute real-time parameter modification by approximating any nonlinear function.

Based on the mathematical model of BIM, this research presents an improved active disturbance rejection control (IADRC) approach. An error integral has been included in the nonlinear state error feedback (NLSEF) of the ADRC to enhance the controlled system's steady-state ability. Additionally, the conventional *fal* function is replaced with a smooth *newfal* function. The derivability, continuity, and smoothness at the origin of this nonlinear function surpass those of the classic nonlinear function. Simultaneously, the enhanced ADRC's parameters are automatically adjusted by the utilization of the self-learning and self-adaptation abilities of the RBFNN. The modeling and experimental findings demonstrate that the IADRC technique, as described in this study, enhances the reaction time, levitation performance, and resistance to interference of the BIM control system.

2. WORKING PRINCIPLE AND MATHEMATICAL MODEL OF THE BIM

2.1. Operational Principle of the BIM

The interaction between the two winding structures leads to a coupling effect that disrupts the consistency of the magnetic field. It is a condition for the realization of the formation of a controllable levitation force in the BIM when the two sets of winding pole pairs of the BIM stator satisfy $P_1 = P_2 \pm 1$; the angular frequency satisfies $\omega_1 = \omega_2$; and the magnetic field generated by the torque winding and the magnetic field generated by the levitation force winding are in the same direction. Fig. 1 depicts the formation principle of levitation force in the BIM. Torque winding and suspension winding are denoted by subscripts 1 and 2, respectively. Two symmetric flux chains, ψ_1 and ψ_2, are produced by applying current I_1 to the torque winding and current I_2 to the levitation winding, respectively. The two magnetic field types are combined within the motor, resulting in an increase in magnetic field density. The motor combines these two magnetic field types, resulting in a rise in magnetic field density along the positive y-axis and a reduction along the negative y-axis. A levitation force, F_y, is generated in the positive y-direction as a result of the asymmetry of the magnetism density in the air gap. The suspension force on the rotor of the motor can be controlled by adjusting the size and phase of the levitation winding current, resulting in a steady suspension of the rotor [2].

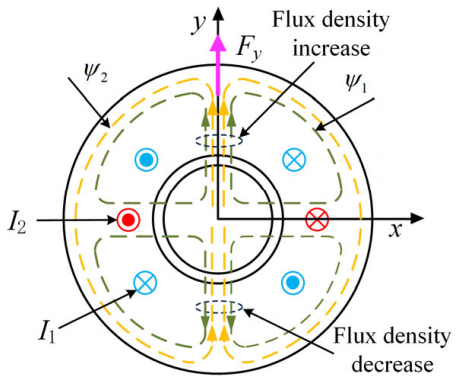

FIGURE 1. Generation principle of levitation force in the BIM.

2.2. Mathematical Model of the BIM

It is imperative to make the following assumptions while creating a mathematical model of the BIM.

(1) Exclude the effects of eddy currents and core losses.

(2) Disregard the impact of magnetic saturation on BIM.

(3) The windings of the BIM are presumed to be evenly distributed in space, and the magnetomotive force of the BIM is sinusoidal.

The radial force component of the suspension section for the BIM system may be mathematically represented as [4]:

$$\begin{cases} F_x = K\left(i_{2sd}\psi_{1d} + i_{2sq}\psi_{1q}\right) \\ F_y = K\left(i_{2sq}\psi_{1d} - i_{2sd}\psi_{1q}\right) \\ K_M = \frac{\pi P_1 P_2 L_{2m}}{18 l_1 r_1 \mu_0 N_1 N_2} \\ K_L = \frac{P_1 N_2}{2 r_1 N_1} \\ K = K_M + K_L \end{cases} \tag{1}$$

where ψ_{1d} and ψ_{1q} denote the air-gap flux chain on the d-q axis, respectively; I_{2sd} and I_{2sq} are the components of the stator current of the suspension winding in the d-q axis, respectively; K_M is the Maxwell's force constant; K_L is the Lorentz's force

constant; F_x and F_y are the components of the levitation force in the x and y directions for the BIM, respectively; l_1 is the effective length of the core; r is the rotor's outer diameter; and N_1 and N_2 are the effective numbers of turns of the torque and suspension force windings, respectively.

The equation of motion for the rotor portion of the BIM may be represented as [7]:

$$\begin{cases} F_x = F_{zx} + F_{sx} - m\ddot{x} \\ F_y = F_{zy} + F_{sy} - m\ddot{y} \\ T_e = \frac{J}{P_1}\frac{d\omega_r}{dt} + T_L \end{cases} \tag{2}$$

where m is the rotor's mass; T_L is the load torque; J is the moment of inertia; F_{zx} and F_{zy} are the outer disturbing force components on the x and y axes, respectively; F_{sx} and F_{sy} are the imbalanced electromagnetic pulling forces on the x and y axes, respectively.

The two winding structures of the BIM are interconnected in a coupling connection. When the BIM is controlled directionally based on the air gap magnetic field:

$$\psi_{1d} = \psi_1, \quad \psi_{1q} = 0 \tag{3}$$

The torque equation may be converted into:

$$T_e = P_1\psi_1 i_{1sq} \tag{4}$$

The suspension force equation may be converted into [8]:

$$\begin{cases} F_x = Ki_{2sd}\psi_1 \\ F_y = Ki_{2sq}\psi_1 \end{cases} \tag{5}$$

Hence, the torque of the BIM is regulated by the current flowing through the torque winding, while the levitation force of the BIM is governed by the current flowing through the suspension winding.

3. DESIGN OF THE STANDARD ADRC IN THE BIM CONTROL SYSTEM

The standard ADRC has three components: Track Differentiator (TD), Nonlinear State Error Feedback, and Extended State Observer. The controller employs the ESO to gauge and counterbalance unknown disruptions in intricate nonlinear control systems, therefore enhancing the system's resilience to disturbances [16].

3.1. Design of the Torque ADRC

This study specifically addresses the closed-loop control of the BIM. In order to do this, a first-order torque ADRC controller is constructed for the torque system. Firstly, Equations (2) and (4) are utilized to get the velocity state equation in the following manner:

$$\dot{\omega}_r = \frac{P_1^2}{J}\psi_1 i_{1sq} - \frac{P_1}{J}T_L \tag{6}$$

Based on the above equation, assuming that the total perturbation of the velocity equation of state is $-\frac{P_1}{J}T_L$, denoted as $\omega(t)$, Equation (6) can be rewritten as:

$$\dot{\omega}_r = \frac{P_1^2}{J}\psi_1 i_{1sq} + w\left(t\right) \tag{7}$$

The ESO of first-order torque ADRC for the BIM can be designed as:

$$\begin{cases} e_1 = \hat{\omega}_r - \omega_r \\ \dot{\hat{\omega}}_r = \hat{w}\left(t\right) - \beta_1 fal\left(e_1, \alpha_1, \delta_1\right) + \frac{P_1^2}{J}\psi_1 i_{1sq} \\ \dot{\hat{w}}\left(t\right) = -\beta_2 fal\left(e_1, \alpha_1, \delta_1\right) \end{cases} \tag{8}$$

where $\hat{\omega}_r$ is the estimated signal of the feedback speed; e_1 is the error signal; $\hat{w}(t)$ is the estimated value of the overall perturbance $w(t)$; the ESO's output error correction gains are denoted by β_1 and β_2; α_1 and δ_1 are adjustable parameters.

The *fal* function is a nonlinear function with the following definition:

$$fal\left(\varepsilon, \alpha, \xi\right) = \begin{cases} \frac{\varepsilon}{\xi^{1-\alpha}}, & |\varepsilon| \le \xi \\ |\varepsilon|^{\alpha}\,\mathrm{sign}\left(\varepsilon\right), & |\varepsilon| > \xi \end{cases} \tag{9}$$

The torque track differentiator in the BIM system can be constructed as:

$$\begin{cases} e_0 = v_1 - \omega_r^* \\ \dot{\omega}_r^* = -rfal(e_1, \alpha_1, \delta_1) \end{cases} \tag{10}$$

where ω_r^* is the given velocity signal; v_1 is the tracking signal of velocity ω_r^*; $\dot{\omega}_r^*$ is the differential signal of the given signal; r is the velocity factor, the bigger r, the higher the tracking speed.

The NLSEF of torque ADRC in the BIM system can be designed:

$$\begin{cases} e = v_1 - \hat{\omega}_r \\ e_0 = \int_0^t e dt \\ i_{s1q0} = k_1 fal\left(e_0, \alpha_1', \delta_1'\right) + k_2 fal\left(e, \alpha_1', \delta_1'\right) \end{cases} \tag{11}$$

where $\hat{\omega}_r$ is the estimated signal of the feedback speed ω_r; e_0 is the integral of the error signal; k_1 and k_2 are the regulator gains of the NLSEF.

3.2. Design of the Suspension ADRC

The ADRC controllers in the x-axis as well as y-axis directions of the BIM suspension system exhibit comparable designs. For the x-axis direction, the equation of state for the x-axis may be derived from the above Equation (2):

$$\begin{cases} \dot{x}_1 = x_2 \\ \dot{x}_2 = \frac{k_s}{m}x_1 + \frac{1}{m}F_{zx} - \frac{1}{m}F_x \\ y = x_1 \end{cases} \tag{12}$$

where k_s is the rigidity of radial displacement; the x-axis displacement signal is denoted by x_1; and the differential signal corresponding to that displacement is represented by x_2.

The overall perturbation in the equation for x-axis displacement is defined by the imbalanced magnetic pull force F_{sx} and

external disturbance force F_{zx} along the x-axis. This is further expanded to include a new state variable, denoted as g_3.

$$g_3 = \frac{1}{m} F_{sx} + \frac{1}{m} F_{zx} \tag{13}$$

If we set $\dot{g}_3 = g(t)$, the original system will become linear:

$$\begin{cases} \dot{x}_1 = x_2 \\ \dot{x}_2 = g_3 - \frac{1}{m} F_x \\ \dot{g}_3 = g(t) \\ y = x_1 \end{cases} \tag{14}$$

Thus, the ESO can be formulated as:

$$\begin{cases} e_2 = z_1 - x_1 \\ \dot{z}_1 = z_2 - \beta_{01} e_2 \\ \dot{z}_2 = z_3 - \frac{1}{m} F_x - \beta_{02} \mathit{fal}(e_2, \alpha_{01}, \delta_2) \\ \dot{z}_3 = -\beta_{03} \mathit{fal}(e_2, \alpha_{02}, \delta_2) \end{cases} \tag{15}$$

where z_1 represents the estimated signal of the x-axis displacement x_1; z_2 is the differential signal of the x-axis displacement estimated value; z_3 is the estimated signal of the overall perturbation estimated in real-time; and β_{01}, β_{02}, β_{03}, α_{01}, α_{02}, and δ_2 are the ESO parameters to be set.

The TD is intended to plan the transition procedure for the specified displacement. It can be designed as:

$$\begin{cases} gh = fhan(v_1(m) - x^*, v_2(m), r_0, h_0) \\ v_1(m+1) = x_1(m) + hx_2(m) \\ v_2(m+1) = x_2(m) + hgh \end{cases} \tag{16}$$

where x^*, v_1, and v_2 are the given rotor displacement signal, actual displacement signal, and its differential signal, respectively; r_0 and h_0 are the function control parameters; and h is the sampling period. The tracking speed increases with increasing r_0, while the filtering effect improves with increasing h.

The NLSEF for the second order suspended ADRC may be formulated as:

$$\begin{cases} e_1 = v_1 - z_1 \\ e_2 = v_2 - z_2 \\ F_{x0} = w_1 \mathit{fal}(e_1, \alpha'_{01}, \delta'_2) + w_2 \mathit{fal}(e_2, \alpha'_{02}, \delta'_2) \end{cases} \tag{17}$$

where w_1, w_2, α'_{01}, α'_{02}, and δ'_2 are the NLSEF's adjustable parameters, and empirical method was used in the selection of these parameters.

4. DESIGN OF THE IMPROVED ADRC

The proposed IADRC, as outlined in this study, has two distinct components: An enhanced control algorithm for the NLSEF and an improved nonlinear *fal* function.

4.1. Improvement of the NLSEF

The adjustable parameters k_{N1} and k_{N2} in the NLSEF correspond to the proportional and differential coefficients in conventional PID controllers. The proportional link accurately represents the error signal of the regulated system in direct proportion. The differential link can accurately indicate the direction of the erroneous signal's change and provide a prompt and efficient correction signal, therefore enhancing the system's reaction time. Increasing the proportionality coefficient k_{N1} of NLSEF can therefore reduce steady-state error and enhance tracking accuracy, but it will also increase the overshooting amount and destroy the dynamic stability of the controlled system. Increasing the differential coefficient k_{N2} of NLSEF can improve the dynamic performance and response speed, but it will also amplify the high frequency noise. Thus, in line with the PID control theory, this work enhances the NLSEF of the ADRC by including the integral of the input error into the first stage system, and it can greatly enhance the controlled system's stable state performance. The state error, together with its integral and differential components, is integrated into the compensated control variable u_0 of the controlled system. As a result, the enhanced NLSEF may be mathematically represented as:

$$\begin{cases} e_1 = v_1 - z_1 \\ e_2 = v_2 - z_2 \\ e_3 = \int_0^t e_1(\tau)\, d\tau \\ fn_1 = \mathit{fal}(e_1, \alpha_{N1}, \delta_N) \\ fn_2 = \mathit{fal}(e_2, \alpha_{N2}, \delta_N) \\ fn_3 = \mathit{fal}(e_3, \alpha_{N3}, \delta_N) \\ u_0 = k_{N1} fn_1 + k_{N2} fn_2 + k_{N3} fn_3 \\ u = u_0 - \frac{z_3}{b_0} \end{cases} \tag{18}$$

where k_{N1}, k_{N2}, and k_{N3} are the gain factors, which correspond to the proportional gain, differential gain, and integral gain in the PID controllers. Augmenting the proportional gain factor can expedite the transition phase and enhance the precision of observations; however, it will also amplify the overshoot. Augmenting the differential gain factor improves the system's dynamic performance and reaction time, but it concurrently increases the noise. Augmenting the integration gain factor can enhance the system's steady-state performance, but it will affect the dynamic process.

4.2. Improvement of the *fal* Function

From the expression of the function *fal*, it can be seen that the smaller the value of α is, the more obvious the smoothness of the traditional *fal* function is, corresponding to a greater degree of nonlinearity. As ξ increases, the linear interval of the traditional *fal* function increases. Therefore, when $|\varepsilon| = \xi$, the traditional *fal* function is not smooth. At this point, the derivative of the conventional *fal* function suddenly changes, resulting in poor performance of the control system. When $|\varepsilon| > 1$, a larger value of α will lead to an increase in the output signal of the control system. Therefore, taking into account ADRC's limitation on the relationship between error and control gain,

the traditional *fal* function is improved according to the following requirements, so that the improved *fal* function is smooth and differentiable in the whole real number domain.

(1) When $|e| = \delta$, the improved *fal* function should be differentiable and continuous;

(2) The improved *fal* function should ensure that the function curve at the origin remains continuous and relatively smooth;

(3) When the control system error is large, the system gain should be small to achieve better control performance.

For the error ε, $\sin\varepsilon$ has better smoothness than ε, and secondly $\arctan\varepsilon$ has better convergence than ε^3. Therefore, at $|\varepsilon| \le \xi$, the improved *fal* function is designed by using the sine function and inverse tangent function for interpolation fitting according to the following method:

$$newfal\left(\varepsilon,\alpha,\xi,\eta\right) = u\sin\varepsilon + v\varepsilon^2 + w\arctan\varepsilon \tag{19}$$

where u, v, and w are the gain coefficients corresponding to the error combinations; η is a constant.

Due to the inherent properties of sine and inverse tangent functions, superior control performance can be achieved using interpolated fitting of sine and inverse tangent functions compared to conventional *fal* functions, while ensuring the function remains continuous and differentiable during the interval. As a result, the following prerequisites need to be satisfied in order for the interpolated *newfal* function to be continuously differentiable:

$$\begin{cases} newfal\left(\varepsilon,\alpha,\xi,\eta\right) = \xi^{\alpha}, & \varepsilon = \xi \\ newfal\left(\varepsilon,\alpha,\xi,\eta\right) = -\xi^{\alpha}, & \varepsilon = -\xi \\ newfal'\left(\varepsilon,\alpha,\xi,\eta\right) = \alpha\xi^{\alpha-1}, & \varepsilon = \xi \\ newfal'\left(\varepsilon,\alpha,\xi,\eta\right) = -\xi^{\alpha}, & \varepsilon = -\xi \end{cases} \tag{20}$$

According to the previous equation, the coefficients corresponding to the errors can be expressed as:

$$\begin{cases} u = \frac{\xi^{\alpha} - \alpha\xi^{\alpha-1}\cdot\left(1+\xi^2\right)\cdot\arctan\xi}{\sin\xi - \arctan\xi\cdot\cos\xi\cdot\left(1+\xi^2\right)} \\ v = 0 \\ w = \frac{\left(\alpha\xi^{\alpha-1}\cdot\sin\xi - \cos\xi\cdot\xi^{\alpha}\right)\left(1+\xi^2\right)}{\sin\xi - \arctan\xi\cdot\cos\xi\cdot\left(1+\xi^2\right)} \end{cases} \tag{21}$$

By introducing a constant η as a constraint factor, the *newfal* function can keep the gain small by adjusting η when the error is large. Thus, when $\xi < |\varepsilon| \le \eta$ is used, the conventional *fal* function remains unchanged. When $|\varepsilon| > \eta$, the *newfal* function is expressed as:

$$newfal\left(\varepsilon,\alpha,\xi,\eta\right) = |\eta|^{\alpha}\,\mathrm{sign}\left(\varepsilon\right) \tag{22}$$

Therefore, based on the above analysis, the improved nonlinear *fal* function designed in this paper can be expressed as:

$$newfal(\varepsilon,\alpha,\xi,\eta) = \begin{cases} u\sin\varepsilon + w\arctan\varepsilon, & |\varepsilon| \le \delta \\ |\varepsilon|^{\alpha}\,\mathrm{sign}\left(\varepsilon\right), & \delta < |\varepsilon| \le \eta \\ |\eta|^{\alpha}\,\mathrm{sign}\left(\varepsilon\right), & |\varepsilon| > \eta \end{cases} \tag{23}$$

4.3. Parameter Self-Tuning Based on the RBFNN

Both the ADRC structure for the BIM's speed system and its levitation system have been improved. The IADRC controller's primary ESO parameters are changed using the RBFNN to enhance the system's capacity for anti-disturbance and more accurately estimate the overall perturbation of the controlled system. This improves the BIM system's real-world performance in both the static and dynamic domains.

The RBFNN's input layer vector information is denoted by $X = [e_1,\ y^*,\ y]$, where e_1 denotes the observation error; Here, y^* denotes the input value, and y denotes the feedback value. Therefore, the error approximation indicator function of RBFNN can be written in the following manner:

$$E\left(m\right) = \frac{\left[y^*\left(m\right) - y\left(m\right)\right]^2}{2} = \frac{e_1^2\left(m\right)}{2} \tag{24}$$

The hidden layer of the network's radial basis vector information is represented by $H = [h_1, h_2, ..., h_m]$. Because of its exceptional performance, the hidden layer's radial basis function is chosen to be a Gaussian function. This function's equation is as follows:

$$h_i\left(\|X - C_i\|\right)\exp\left(-\frac{\|X - C_i\|^2}{2b_i^2}\right),\ i = 1, 2, \cdots, m \tag{25}$$

where $C_i = [c_{i1}, c_{i2}, ..., c_{in}]$ is the hidden layer neuron's Gaussian centroid vector; $B_i = [b_{i1}, b_{i2}, ..., b_{in}]$ is the hidden layer node's base-width length vector, which controls the neuron's sensitivity; $\|\cdot\|$ is the hidden layer node's Euclidean vector paradigm; and the weight vector is represented by $W = [w_1, w_2, ..., w_m]$. The RBFNN's output layer can be shown as follows:

$$y_j = \sum_{j=1}^{m} w_j h_j,\ \ j = 1, 2, ..., m \tag{26}$$

The core of the design of the RBFNN model is to determine the parameters of the implicit layer basis functions c_i, b_i, and connection weights w_i. The gradient descent approach is used to learn and train the network model parameters as well as to modify the network parameters. The following is the precise training formula:

$$\begin{cases} \Delta c_i\left(m\right) = -\eta\frac{\partial E(m)}{\partial_i(m-1)} \\ = \eta e_j\left(m\right) w_i\left(m-1\right) h_i\left(x\left(m\right)\right)\frac{x(m)-c_i(m-1)}{b_i^2(m-1)} \\ c_i\left(m\right) = c_i\left(m-1\right) + \Delta c_i\left(m\right) \\ +\alpha_1\left(c_i\left(m-1\right) - c_i\left(m-2\right)\right) \\ \Delta b_i\left(m\right) = -\eta\frac{\partial E(m)}{\partial b_i(m-1)} \\ = \eta e_j(m) w_i(m-1) h_i\left(x(m)\right)\frac{\|x(m)-c_i(m-1)\|^2}{b_i^3(m-1)} \\ b_i\left(m\right) = b_i\left(m-1\right) + \Delta b_i\left(m\right) \\ +\alpha_1\left(b_i\left(m-1\right) - b_i\left(m-2\right)\right) \\ \Delta w_i\left(m\right) = -\eta\frac{\partial E(m)}{\partial w_i(m-1)} = \eta e_j\left(m\right) h_i\left(x\left(m\right)\right) \\ w_{ij}\left(m\right) = w_{ij}\left(m-1\right) + \Delta w_{ij}\left(m\right) \\ +\alpha_1\left(w_{ij}\left(m-1\right) - w_{ij}\left(m-2\right)\right) \end{cases} \tag{27}$$

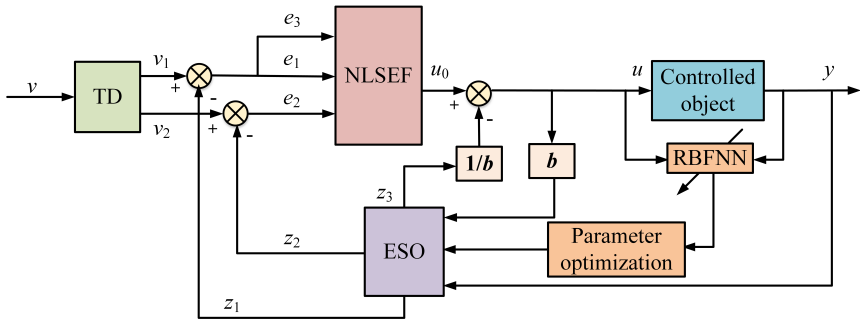

FIGURE 2. Parameter self-tuning structure diagram of the IADRC.

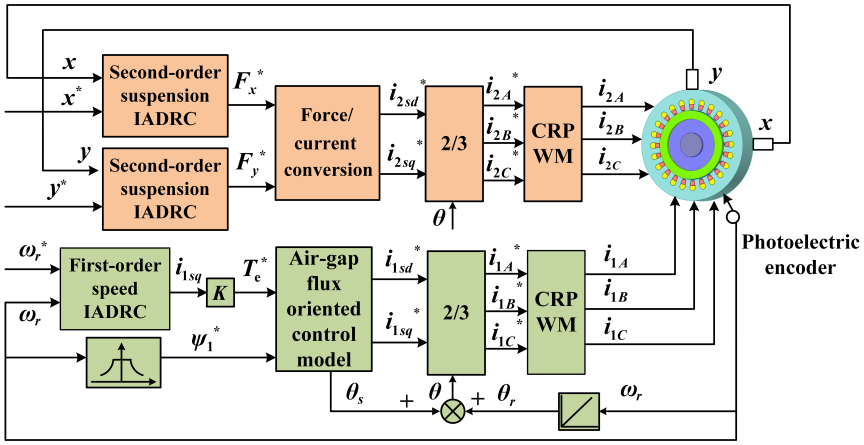

FIGURE 3. The general block diagram of the BIM control system.

where α_1 represents the momentum factor and corresponds to the interval [0, 1], and η represents the learning rate.

The suspension system's ADRC controller's ESO settings are changed to improve the BIM operating system's control effectiveness, with an example provided by the 3-6-1 type three-layer RBFNN structure in the x-axis direction. The structure of the self-adjustment of the IADRC parameters is illustrated in Fig. 2.

The optimization step may be explained as follows:

Step 1: The architectures of IADRC and RBFNN are established, and the corresponding parameters are initialized;

Step 2: The anticipated control input, achieved control outcome, and related control quantity are acquired;

Step 3: The difference between the RBFNN's output value and the real control output is computed. Proceed to step 5 if the variance meets the performance index; if not, proceed to step 4;

Step 4: The network center vector, base width vector, and weight vector of the RBFNN are altered;

Step 5: The computation of the Jacobi matrix information is performed.

Step 6: The ESO parameters β_{01}, β_{02}, and β_{03} are adjusted by the gradient descent method to output the optimal parameters of the controller;

Step 7: The control quantity is computed and produced based on the optimization outcomes;

Step 8: Verify whether there is a discrepancy between the observed control outcome and the anticipated input. If there is, continue to step 2. Alternatively, conclude.

The controlled object's Jacobi information is obtained by RBFNN learning, where RBFNN modifies the extended state observers β_{01}, β_{02}, and β_{03} in the IADRC. Similarly, the parameters β_1 and β_2 of the ESO in the IADRC in the first-order torque system's IADRC can be tuned online.

5. SIMULATION AND EXPERIMENTAL RESULTS ANALYSIS OF THE CONTROL SYSTEM

To confirm the efficacy of the recommended approach in the BIM control system, a simulation model that utilizes air-gap flux orientation control of the BIM is built in MATLAB/Simulink. The efficiency of the conventional ADRC controllers as well as the IADRC controllers in BIM control has been demonstrated by simulation. The overall structure of the designed BIM control system is shown in Fig. 3. The BIM simulation parameters are displayed in Table 1.

5.1. Simulation Results and Discussions

Figure 4 displays the rotational velocity response characteristics of the BIM under the two control strategies. By setting the target speed of BIM to 3000 r/min, both ADRC and IADRC can ultimately reach a stable condition. When the ADRC tech-

TABLE 1. The parameter of the BIM.

Parameter	Torque winding	Suspension Winding
Core length (m)	0.105	0.105
Rated power (kW)	1	0.5
Rotor mass (g)	2850	2850
Rated current (A)	2.86	2.86
Moment of inertia (g·m)^2	7.69	7.69
Stator and rotor mutual inductance (H)	0.15856	0.00932
Rotor resistance (Ω)	11.48	0.075
Stator resistance (Ω)	2.01	1.03
Rotor leakage inductance (H)	0.00922	0.00542
Stator leakage inductance (H)	0.00454	0.00267
stator outer diameter (mm)	128	128
rotor outer diameter (mm)	82	82
stator inner diameter (mm)	83	83
stator inner diameter (mm)	30	30

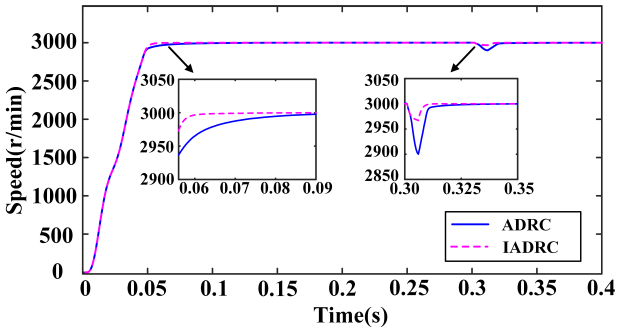

FIGURE 4. Control result of speed part.

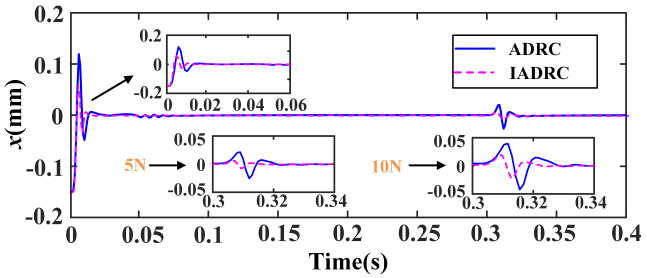

FIGURE 5. Control results of radial displacement in the x-direction of the suspended part.

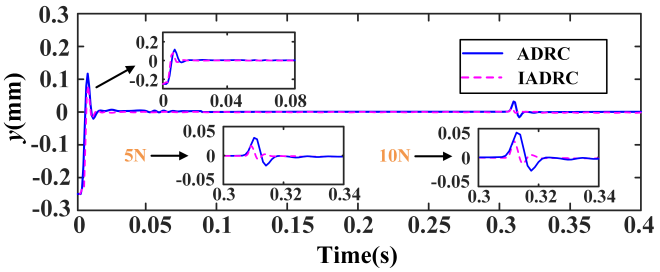

FIGURE 6. Control results of radial displacement in the y-direction of the suspended part.

nique is used, the BIM system is able to reach a stable rotational state in just 0.09 seconds. The BIM speed, while using IADRC, achieves the target speed in 0.065 seconds and is not beyond it. The data show that the initial performance of BIM under IADRC is better.

At $t = 0.3$ s, a 9 N·m load was applied abruptly, the rotating speed decreased by 98 r/min using the ADRC approach and returned to a stable speed within 0.025 seconds. However, the velocity of the BIM using the IADRC technique was reduced by 35 r/min and then returned to the desired velocity after 0.011 seconds. In summary, the superiority of the recommended IADRC strategy is visible in terms of its anti-disturbance performance.

Figure 5 shows the radial displacement control characteristics of the BIM in the x-axis direction under the two strategies. According to Fig. 5, the rotor's center of mass is positioned at the initial location of 0.15 mm on the x-axis, and the traditional ADRC algorithm achieves the desired value in around 0.09 seconds. The radial displacement reaches a maximum amplitude of 0.12 mm. The control performance of the BIM is much im-

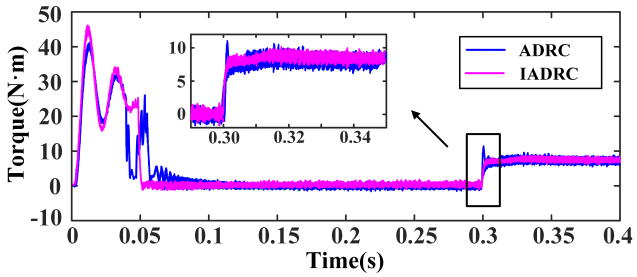

FIGURE 7. Torque output characteristics under two methods.

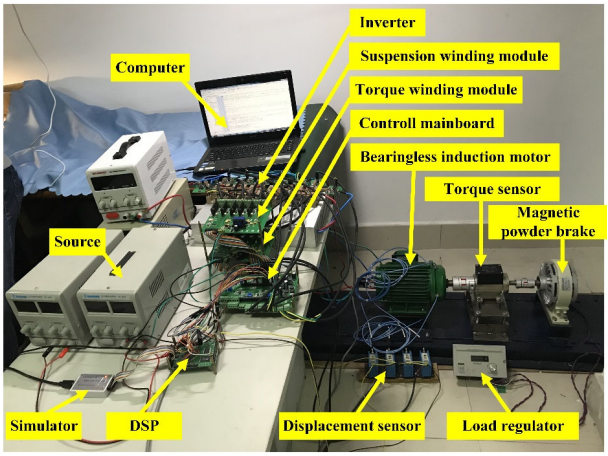

FIGURE 8. Experiment platform of the BIM.

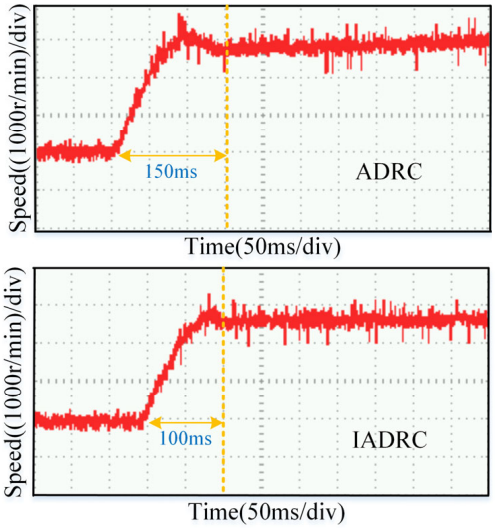

FIGURE 9. Experimental graph of rotational speed under two control methods.

proved by optimizing the control law and the nonlinear function of the NLSEF and by fine-tuning the major control parameters of the IADRC controller using the RBFNN. The control performance is much enhanced while using IADRC. In Fig. 5, the radial displacement of the IADRC experiences a 50% reduction in its maximum amplitude compared to the traditional ADRC. Furthermore, the IADRC is significantly outperformed in terms of the time needed to achieve a stable condition compared to the traditional ADRC. A sudden 5N disturbance force is applied at 0.3 seconds to assess the robustness of the two controllers. The findings demonstrate that the ADRC displays oscillations characterized by a maximum amplitude of radial displacements of 25 μm and a regulation time of 0.022 s. The IADRC has a maximum amplitude of radial displacements of 10 μm and a regulation time of 0.018 s. In addition, when the BIM is suddenly subjected to a disturbance force of 10N at 0.3 s, the maximum amplitude of the radial displacement of the rotor in the x-axis direction of the BIM is 44 μm with a regulation time of 0.038 s under the ADRC control method, and the maximum amplitude of the radial displacement of the rotor is 26 μm with a regulation time of 0.027 s under the IADRC control method. Therefore, this study introduces a suggestion for improving the framework of the traditional ADRC. The key variables of ESO in the improved ADRC are fine-tuned by the use of the RBFNN. The IADRC method improves the ability of the BIM control system to resist interference.

Figure 6 shows the radial displacement control features of the BIM in the y-axis direction for both techniques. Like the x-axis direction, the IADRC method accelerates the process of reaching a steady state and decreases the maximum amplitude of the radial displacement. Conventional ADRC has relatively weak control performance and immunity to interference ability. As a result, the IADRC in complex system control can enhance system performance and produce favorable control outcomes.

Figure 7 illustrates the torque control features of the BIM using two distinct methodologies. The torque of the BIM under the IADRC method drops to 0 faster and outperforms the starting performance of ADRC. Under the IADRC approach, the motor's torque stabilizes more quickly and exhibits reduced torque pulsation compared to the ADRC method when a 9 N·m load is suddenly introduced. Additionally, this demonstrates that the IADRC has exceptional initial performance and resilience against load perturbations. Due to the structural improvement of ADRC and the optimization of key parameters based on the RBFNN, the IADRC method has less oscillation phenomenon during the whole control process and is even better in terms of the stability of the BIM operation system.

5.2. Test Results and Discussions

As seen in Fig. 8, a BIM prototype and an experimental platform are constructed to confirm the viability and effectiveness of the proposed control strategies in actual application scenarios. In the experiments, TMS320F2812 is used as the DSP chip for BIM control, and the sampling frequency is set to 20 kHz.

The control performance of the velocity and levitation part of the BIM under the ADRC and IADRC methods are experimentally verified on the prototype testbed as shown in Fig. 8.

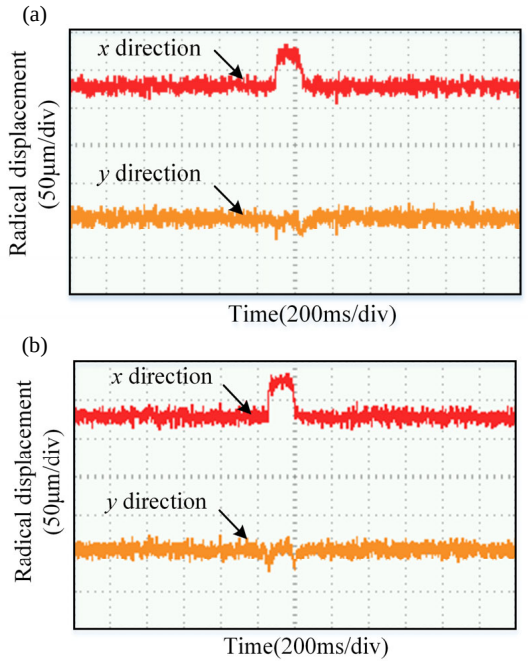

FIGURE 10. Displacement diagram under two control methods. (a) Radial displacement of the rotor under ADRC. (b) Rotor radial displacement under IADRC.

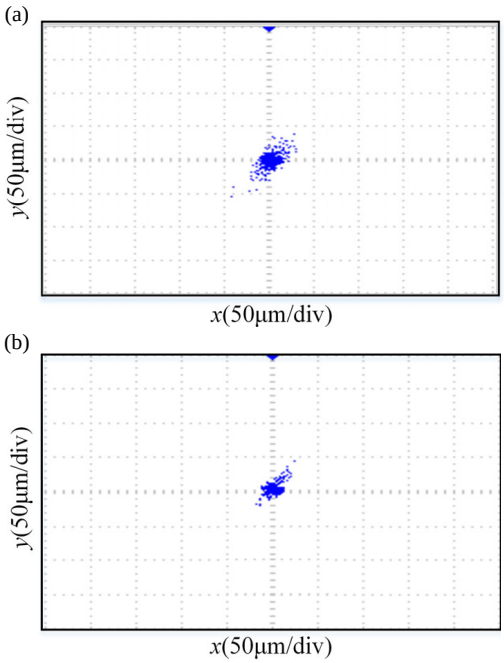

FIGURE 11. Experimental diagrams of rotor centroid trajectories under two control methods. (a) Rotor center of mass trajectory under ADRC. (b) Rotor center of mass trajectory under IADRC.

Figure 9 illustrates that the torque component of the BIM achieves rapid attainment of the desired speed with an adjustment time of 100 ms when using the IADRC. The standard ADRC has a similar adjustment time of 150 ms, which is attributed to the restrictions of parameter invariance. As seen from Figs. 10 and 11, when comparing the IADRC technique to the standard ADRC approach, it is seen that the IADRC method exhibits less volatility, enhanced resistance to external disturbances, and increased stability of the rotor's operation near the equilibrium position. As a result, the experimental results indicate that the BIM system shows exceptional dynamic performance when employing the IADRC control approach.

6. CONCLUSION

To enhance the quickness of responsiveness and suspension performance, this research proposes an IADRC technique to enhance the disturbance immunity of the BIM control system. The following inferences can be made based on the analysis of the theoretical and simulated experiment results.

(1) Using the RBFNN's approximation ability to any nonlinear function, the setting variables of the ESO in the IADRC controller are self-tuned, while the NLSEF and nonlinear *fal* functions in the standard ADRC structure are enhanced.

(2) The findings of the simulation confirm that the suggested approach is both workable and efficient. The suggested IADRC technique enhances the BIM control system's response time and anti-interference capability compared to the standard ADRC.

(3) The experimental findings demonstrate that compared to the standard ADRC, the suggested IADRC approach reduces the reaction time of BIM speed by 33%, resulting in a decreased fluctuation in the centroid of the rotor. Hence, the approach described in this study can improve both the rate of response and the levitation properties of the BIM.

REFERENCES

[1] Chen, J., Y. Fujii, M. W. Johnson, A. Farhan, and E. L. Severson, "Optimal design of the bearingless induction motor," *IEEE Transactions on Industry Applications*, Vol. 57, No. 2, 1375–1388, 2020.

[2] Ding, Q., Z. Yang, X. Sun, and C. Lu, "Stepless speed regulation study of a wound pole-fixed bearingless induction motor with three windings," *IEEE Transactions on Industrial Electronics*, Vol. 70, No. 7, 6724–6734, 2023.

[3] Asama, J. and A. Chiba, "Three-coil combined winding configuration for a 2-DOF actively controlled bearingless permanent magnet motor," *IEEE Transactions on Industry Applications*, Vol. 57, No. 6, 6765–6773, 2021.

[4] Yang, Z., C. Sun, X. Sun, and Y. Sun, "An improved dynamic model for bearingless induction motor considering rotor eccentricity and load change," *IEEE Transactions on Industrial Electronics*, Vol. 69, No. 4, 3439–3448, Apr. 2022.

[5] Rodriguez, E. F. and J. A. Santisteban, "An improved control system for a split winding bearingless induction motor," *IEEE Transactions on Industrial Electronics*, Vol. 58, No. 8, 3401–3408, 2011.

[6] Yang, Z., Q. Ding, X. Sun, C. Lu, and H. Zhu, "Speed sensorless control of a bearingless induction motor based on sliding mode observer and phase-locked loop," *ISA Transactions*, Vol. 123, 346–356, Apr. 2022.

[7] Bu, W., F. Zhang, F. He, L. Sun, and Y. Qiao, "Neural network inverse system decoupling fuzzy self-tuning proportional-derivative control strategy of a bearingless induction motor," *Proceedings of the Institution of Mechanical Engineers, Part I: Journal of Systems and Control Engineering*, Vol. 235, No. 7,

1113–1124, Aug. 2021.

[8] Li, K., F. Ling, X. Sun, Y. Cai, D. Zhao, and Z. Yang, "Displacement sensorless control for bearingless induction motor drives based on the MRAS method," *International Journal of Applied Electromagnetics and Mechanics*, Vol. 62, No. 4, 787–805, 2020.

[9] Wang, G., R. Liu, N. Zhao, D. Ding, and D. Xu, "Enhanced linear ADRC strategy for HF pulse voltage signal injection-based sensorless IPMSM drives," *IEEE Transactions on Power Electronics*, Vol. 34, No. 1, 514–525, 2019.

[10] Zheng, Y., R. Dai, and Z. Zhou, "Design of torque system for electric bicycle based on fuzzy PID," *The Journal of Engineering*, Vol. 2019, No. 23, 8710–8714, 2019.

[11] Qi, Z., Q. Shi, and H. Zhang, "Tuning of digital PID controllers using particle swarm optimization algorithm for a CAN-based DC motor subject to stochastic delays," *IEEE Transactions on Industrial Electronics*, Vol. 67, No. 7, 5637–5646, 2019.

[12] Chen, P. and Y. Luo, "Analytical fractional-order PID controller design with bode's ideal cutoff filter for PMSM speed servo system," *IEEE Transactions on Industrial Electronics*, Vol. 70, No. 2, 1783–1793, 2022.

[13] Vinh, V. Q. and V. T. Ha, "Improved torque ripple of switched reluctance motors using sliding mode control for electric vehicles," *Engineering Technology & Applied Science Research*, Vol. 13, No. 1, 10 140–10 144, Feb. 2023.

[14] Morsi, A., H. S. Abbas, S. M. Ahmed, and A. M. Mohamed, "Model predictive control based on linear parameter-varying models of active magnetic bearing systems," *IEEE Access*, Vol. 9, 23 633–23 647, 2021.

[15] Li, K., F. Ling, X. Sun, and Z. Yang, "Decoupling control of bearingless PMSM with LSSVM inverse system and IMC," *International Journal of Applied Electromagnetics and Mechanics*, Vol. 65, No. 4, 715–734, 2021.

[16] Bu, W., F. Zhang, Y. Chen, and X. Zhang, "Fuzzy MRAS rotor resistance identification of BL-IM based on reactive power," *International Journal of Applied Electromagnetics and Mechanics*, Vol. 65, No. 4, 661–680, 2021.

[17] Yang, Z., J. Wu, C. Lu, and D. Wang, "Predictive current control of a bearingless induction motor model based on fuzzy dynamic objective function," *Transactions of the Institute of Measurement and Control*, Vol. 42, No. 16, 3183–3195, Dec. 2020.

[18] Alonge, F., M. Cirrincione, F. D'Ippolito, M. Pucci, and A. Sferlazza, "Active disturbance rejection control of linear induction motor," *IEEE Transactions on Industry Applications*, Vol. 53, No. 5, 4460–4471, 2017.

[19] Han, J., "Active disturbance rejection controller with its application," *Control and Decision*, No. 1, 19–23, 1998.

[20] Zhu, H. and Z. Gu, "Active disturbance rejection control of 5-degree-of-freedom bearingless permanent magnet synchronous motor based on fuzzy neural network inverse system," *ISA Transactions*, Vol. 101, 295–308, Jun. 2020.

[21] Li, K., G. Cheng, X. Sun, D. Zhao, and Z. Yang, "Direct torque and suspension force control for bearingless induction motors based on active disturbance rejection control scheme," *IEEE Access*, Vol. 7, 86 989–87 001, 2019.

[22] Wang, S., H. Zhu, M. Wu, and W. Zhang, "Active disturbance rejection decoupling control for three-degree-of-freedom six-pole active magnetic bearing based on BP neural network," *IEEE Transactions on Applied Superconductivity*, Vol. 30, No. 4, 3603505, Jun. 2020.

[23] Chen, Y. and Y. Zhou, "Active disturbance rejection and ripple suppression control strategy with model compensation of single-winding bearingless flux-switching permanent magnet motor," *IEEE Transactions on Industrial Electronics*, Vol. 69, No. 8, 7708–7719, 2021.

[24] Zhang, C., C. Zhang, L. Li, and H. Liu, "An enhanced nonlinear ADRC speed control method for electric propulsion system: Modeling, analysis, and validation," *IEEE Transactions on Power Electronics*, Vol. 38, No. 4, 4520–4528, Apr. 2023.

[25] Zhang, Y., X. Ruan, L. Hu, L. Li, B. Li, and X. Chen, "Active disturbance rejection control for bearingless permanent-magnet slice motor based on nonlinear phase-locked loop observer," *Proceedings of the Institution of Mechanical Engineers, Part C: Journal of Mechanical Engineering Science*, Vol. 235, No. 19, 3806–3818, 2021.

[26] Wang, Y., S. Fang, and J. Hu, "Active disturbance rejection control based on deep reinforcement learning of PMSM for more electric aircraft," *IEEE Transactions on Power Electronics*, Vol. 38, No. 1, 406–416, 2022.

[27] Shimizu, Y., S. Morimoto, M. Sanada, and Y. Inoue, "Automatic design system with generative adversarial network and convolutional neural network for optimization design of interior permanent magnet synchronous motor," *IEEE Transactions on Energy Conversion*, Vol. 38, No. 1, 724–734, 2022.

[28] Fang, S., Y. Wang, W. Wang, Y. Chen, and Y. Chen, "Design of permanent magnet synchronous motor servo system based on improved particle swarm optimization," *IEEE Transactions on Power Electronics*, Vol. 37, No. 5, 5833–5846, May 2022.

[29] Wang, T., H. Wang, H. Hu, J. Qing, and C. Wang, "Lion swarm optimisation-based tuning method for generalised predictive fractional-order PI to control the speed of brushless direct current motor," *IET Electric Power Applications*, Vol. 16, No. 8, 879–895, 2022.

[30] Ma, T., X. Guo, G. Su, H. Deng, and T. Yang, "Research on synchronous control of active disturbance rejection position of multiple hydraulic cylinders of digging-anchor-support robot," *Sensors*, Vol. 23, No. 8, 4092, 2023.

[31] Than, H. and Y.-S. Kung, "FPGA-realization of an RBF-NN tuning PI controller for sensorless PMSM drives," *Microsystem Technologies*, Vol. 28, 25–38, 2022.

[32] Prakash, A. and C. Naveen, "Combined strategy for tuning sensor-less brushless DC motor using SEPIC converter to reduce torque ripple," *ISA Transactions*, Vol. 133, 328–344, Feb. 2023.

[33] Jie, H., G. Zheng, J. Zou, X. Xin, and L. Guo, "Speed regulation based on adaptive control and RBFNN for PMSM considering parametric uncertainty and load fluctuation," *IEEE Access*, Vol. 8, 190 147–190 159, 2020.